Geosci. Model Dev. Discuss., doi:10.5194/gmd-2016-200, 2016
Manuscript under review for journal Geosci. Model Dev.
Published: 15 September 2016

Geoscientific Model Development Discussions
Open Access

Variational assimilation of IASI SO2 plume height and total-column retrievals in the 2010 eruption of Eyjafjallajökull using the SILAM v5.3 chemistry transport model

Julius Vira[1], Elisa Carboni[2], Roy G. Grainger[3], Mikhail Sofiev[1]

[1] Finnish Meteorological Institute, Erik Palménin aukio 1, FI-00560 Helsinki, Finland
[2] COMET, Atmospheric, Oceanic and Planetary Physics, University of Oxford, Parks Road, Oxford, OX1 3PU, U.K.
[3] National Centre for Earth Observation, Atmospheric, Oceanic and Planetary Physics, University of Oxford, Parks Road, Oxford OX1 3PU, U.K.

Correspondence to: J. Vira, julius.vira@fmi.fi

Abstract

This study focuses on two new aspects on inverse modelling of volcanic emissions. First, we derive an observation operator for satellite retrievals of plume height, and second, we solve the inverse problem using the 4D-Var method. The approach is demonstrated by assimilating IASI SO_2 plume height and total column retrievals in a source term inversion for the 2010 eruption of Eyjafjallajökull. The inversion resulted in temporal and vertical reconstruction of the SO_2 emissions during the 1-20 May, 2010 with formal vertical and temporal resolutions of 500 m and 12 hours.

The plume height observation operator is based on simultaneous assimilation of the plume height and total column retrievals. The plume height is taken to represent the vertical centre of mass, which is transformed into the first moment of mass. This makes the observation operator linear and simple to implement. The necessary modifications to the observation error covariance matrix are derived.

Regularisation by truncated iteration is investigated as a simple and efficient regularisation method for the 4D-Var based inversion. In an experiment with synthetic observations, the truncated iteration was found to perform similarly to the commonly used Tikhonov regularisation. However, the truncated iteration allows the amount of regularisation to be varied a posteriori, without repeating the inversion. For inverting the Eyjafjallajökull SO_2 emission at the temporal and vertical resolution used in this study, the 4D-Var method required about 70% less computational effort than commonly used methods based on performing a separate model simulation for each degree of freedom in the estimated source term.

Compared to the inversion using only total column retrievals, assimilating the plume height resulted in a vertical emission profile more closely matching the ash plume heights observed by radar. The a posteriori source term gave an estimate of 0.29 Tg erupted SO_2 of which 95% was injected below 11 km.

1 Introduction

Sulphur dioxide (SO_2) is one of the major gas-phase species released in volcanic eruptions. Large SO_2 releases pose a hazard to aviation, decrease air quality, and as precursors to sulphate aerosols, have a potential impact the Earth's radiative balance (Bernard and Rose, 1990; Robock, 2000; Schmidt et al., 2015). Volcanic SO_2 plumes can be detected by satellite instruments measuring in either UV or IR wavelengths - however, reliably forecasting the atmospheric transport of volcanic plumes is hindered by the lack of in-situ measurements to characterise the emission fluxes of volcanic species (Carn et al., 2009; Stohl et al., 2011; Zehner, 2012).

While methods based purely on satellite retrievals (Theys et al., 2013 and references therein) exist for inferring the total SO_2 flux for a given eruption, a successful prediction of volcanic tracers generally requires information also on the vertical profile of emissions. An important technique for assessing both vertical and temporal distribution of the emission fluxes is provided by inverse dispersion modelling, first demonstrated for volcanic emissions by Eckhardt et al. (2008).

The previous studies on inverse modelling of volcanic emissions have been based on using total column retrievals of SO_2 or volcanic ash together with a Lagrangian (Kristiansen et al., 2010; Stohl et al., 2011) or Eulerian (Boichu and Clarisse, 2014; Boichu et al., 2013) dispersion models. In addition, Flemming and Inness (2013) devised a trajectory based scheme to evaluate the vertical emission profile, which was used together with assimilation of SO_2 retrievals with the IFS weather prediction system. The previous studies have demonstrated that the vertical distribution of emissions can be inferred from total column retrievals in presence of sufficient vertical wind shear. However, in the case of the Eyjafjallajökull eruption in 2010, both Boichu et al. (2013) and Flemming and Inness (2013) pointed out a lack of wind shear and a subsequent difficulty at estimating the vertical distribution of emissions.

Retrievals of SO_2 plume height have been performed with various satellite instruments (Carboni et al., 2012; Rix et al., 2012). Nevertheless, only a few studies have incorporated these data into models. Wang et al. (2013) derived a three-dimensional SO_2 distribution from retrievals by the Ozone Monitoring Instrument (OMI), and used the distribution to initialize CTM simulations for the 2008 eruption of Kasatochi. Wilkins et al. (2015) used 1D-Var ash retrievals for initialising dispersion simulations. However, neither of the studies used plume height retrievals in inverse modelling of volcanic emissions.

The first objective of the present paper is to assess the usefulness of assimilating SO_2 plume height retrievals from the Infrared Atmospheric Sounding Interferometer (IASI) instrument in a source term inversion. In Section 3.2 we develop an observation operator for the vertical centre of mass. Since the observation operator only depends on the centre of mass and column loading, the vertical profile is only partly constrained. However, in contrast to the previous studies, this approach makes no further assumptions about the shape or thickness of the SO_2 layer. This could be advantageous, since volcanic ash or SO_2 layers vary considerably in depth (Dacre et al., 2014) and can be emitted in multiple, overlapping layers (Kristiansen et al., 2010). In addition, our approach makes full use of the retrieval error estimates provided with the IASI data for both column mass and plume height, including the estimated correlation between plume height and mass errors.

The second objective of this paper is to explore the connection between the source term inversion and the 4D-Var data assimilation widely used in numerical weather prediction. Elbern et al. (2000) showed that the 4D-Var assimilation method (Le Dimet and Talagrand, 1986) can be easily extended into estimating emission fluxes with a chemistry transport model. Under the assumption of a linear dispersion model and observations, the 4D-Var formulation results in a least squares problem similar to that solved by many existing inversion algorithms. However, the iterative solution employed in 4D-Var favours a different regularisation approach, which is discussed in Section 4.

Finally, we test the variational inversion method and assimilation of plume height retrievals for estimating temporal and vertical distribution of SO_2 emission during the 2010 eruption of Eyjafjallajökull. Results of the inversion, presented in Section 5, indicate that assimilation of plume height retrievals results in more vertically concentrated emission profile. In particular, emissions above 8-10 km are reduced substantially, which is consistent with radar-based estimates of the eruption column height.

2 Model setup and observational data

2.1 Dispersion model

The transport and removal of SO_2 was evaluated using the dispersion model SILAM (System for integrated modelling of atmospheric composition; Sofiev et al., 2015, http://silam.fmi.fi) version 5.3. The model includes chemical removal of SO_2 as described by Sofiev (2000) with the OH climatology of Spivakovsky et al. (2000). The computations were driven by the ERA-Interim meteorological reanalysis (Dee et al., 2011) except for evaluating the simulated satellite retrievals described in Section 4, where operational ECMWF forecasts were used.

SILAM includes a variational data assimilation module, which was previously used for assimilation of air quality monitoring data of SO_2 by Vira and Sofiev (2012). This study uses the same assimilation system, but instead of estimating a refinement for a regional emission inventory, we seek to reconstruct the emissions for a single volcanic eruption as a function of time and injection height.

The model was configured for a domain covering 50°E to 30°W and 30°N to 80°N. Horizontal resolution of 0.5° was used for the inversion, while the a posteriori simulations were run with a higher 0.25° resolution. The vertical discretisation consists of 34 terrain-following z-levels with a 500 m resolution at the top of the domain increasing to 50 m near the surface.

2.2 Observations: the IASI dataset

IASI is an infrared Fourier transform interferometer that measures in the spectral range 645–2760 cm^{-1} with spectral sampling of 0.25 cm^{-1} (apodized spectral resolution of 0.5 cm-1) and has global coverage every 12h. The lev1b dataset from EUMETSAT/CEDA archive is used in this study.

Geosci. Model Dev. Discuss., doi:10.5194/gmd-2016-200, 2016
Manuscript under review for journal Geosci. Model Dev.
Published: 15 September 2016

Geoscientific Model Development Discussions

The algorithm and the dataset are explained in more detail by Carboni et al. (2012). The same algorithm has been applied to other volcanic eruptions and successfully compared with other datasets (Carboni et al., 2016; Fromm et al., 2014; Koukouli et al., 2014; Schmidt et al., 2015; Spinetti et al., 2014).

The main points of the retrieval scheme are:

Retrieval are performed for the pixels that were identified by the SO_2 detection scheme (Walker et al 2011, 2012).

All the channels between 1100-1200 and 1300-1410 cm^{-1} are used in the iterative optimal estimation retrieval scheme to obtain SO_2 column amount and altitude of the plume (in pressure, under the assumption that the vertical concentration of SO_2 follows a Gaussian distribution) together with the surface temperature. The scheme determines the column amount and effective altitude of the SO_2 plume with high precision (up to 0.3 DU error in SO_2 amount if the plume is near the tropopause), and it is well suited for plumes in low troposphere.

The IASI SO_2 retrieval is not affected by underlying cloud. If the SO_2 is within or below an ash or cloud layer its signal will be masked and the retrieval will underestimate the SO_2 amount. In the case of ash this is discernible a posteriori by the value of the cost function. The altitude retrieved for the Eyjafjallajökull eruption plume (using same dataset as in this paper) in presence of underlying cloud is consistent with the CALIPSO vertical backscatter profile (Carboni et al 2016, Figs. 1,2,3).

A comprehensive error budget for every pixel is included in the retrieval. This is derived from an error covariance matrix S_ε that is based on the SO_2-free climatology of the differences between the IASI and forward modelled spectra.

Note that the error covariance, S_ε, is defined to represent the effects of atmospheric variability not represented in the forward model, as well as instrument noise. This includes the effects of cloud and trace-gases which are not explicitly modelled. The matrix is constructed from differences between forward model calculations (for clear-sky) and actual IASI observations for wide range of conditions, when we are confident that negligible amounts of SO_2 are present. It follows that a rigorous error propagation, including the incorporation of forward model and forward model parameter error, is built into the system, providing quality control and error estimates on the retrieved state. The retrieval state error covariance matrix, used for the assimilation in this work, is directly provided as output of the retrieval pixel by pixel.

2.3 Inversion experiments

The IASI data were assimilated in inversion experiments for the Eyjafjallajökull (2010) eruption. The eruption has been described in detail by Gudmundsson et al. (2012). The experiments covered the time between 1 and 21 May, 2010, which as shown by Flemming and Inness (2013) included the most significant SO_2 releases.

The emission flux density (kg m^{-1} s^{-1}) was estimated for each model level in steps of 12 hours. The inversions were made with three configurations: with assimilation of both column mass and centre of mass, with assimilation of column mass only, and with assimilation of both column mass and centre of mass but with a simplified formulation for the observation error covariance matrix.

Additionally, Section 4 describes a set of inversion experiments with simulated observations. These experiments were performed with similar configuration as the main experiments, but with a lower vertical resolution of 1 km.

Geosci. Model Dev. Discuss., doi:10.5194/gmd-2016-200, 2016
Manuscript under review for journal Geosci. Model Dev.
Published: 15 September 2016

3 Assimilation and inversion methods

The forward problem for volcanic tracer transport is defined by the advection-diffusion equation: given the emission forcing f, solve

(1) $$\frac{\partial c}{\partial t} + \nabla \cdot (c\mathbf{V}) - \nabla \cdot (K \nabla c) = f(x,t) - s(c,x,t),$$

where c is the tracer concentration, $\mathbf{V}$ is the wind vector, K is the turbulent diffusivity tensor, and $s(c,x,t)$ denotes the chemical and other sinks.

3.1 Variational source term inversion

The inverse problem discussed in this paper is to determine the forcing f, given a set of observations depending on c. We assume that Eq. (1) has been discretised, and following the common notation in data assimilation literature, we denote the tracer concentrations, collectively for all time steps, with the state vector $\mathbf{x}$. The state vector is related to the unknown parameter vector $\mathbf{f}$ by the model operator $\mathcal{M}$. Finally, the vector $\mathbf{y}$ of observations is given by the possibly non-linear observation operator $\mathcal{H}$ as $\mathbf{y} = \mathcal{H}(\mathbf{x}) + \boldsymbol{\varepsilon}$, where $\boldsymbol{\varepsilon}$ denotes the observation error.

If the observation errors follow a multivariate normal distribution with covariance matrix $\mathbf{R}$, then a solution to the inverse dispersion problem can be sought by maximising the likelihood function, which is equivalent to minimising the cost function

(2) $$J(\mathbf{f}) = \frac{1}{2}(\mathbf{y} - \mathcal{H}(\mathbf{x}))^T \mathbf{R}^{-1} (\mathbf{y} - \mathcal{H}(\mathbf{x})),$$

where $\mathbf{x} = \mathcal{M}(\mathbf{f})$. Model errors are not explicitly included in the cost function.

If the model and observation operators are linear, represented by matrices $\mathbf{M}$ and $\mathbf{H}$, then (2) becomes a linear least-squares problem. For volcanic eruptions with a known location, the emission vector $\mathbf{f}$ is zero almost everywhere, which makes it feasible to evaluate the matrix $\mathbf{HM}$ and solve (2) algebraically. This is the basis for inversion methods of Boichu et al. (2013), Eckhardt et al. (2008) and Lu et al. (2016).

As an alternative to the algebraic solution, the minimisation problem (2) can be solved with gradient-based, iterative algorithms, which avoids evaluating the matrix $\mathbf{HM}$. In this study, the cost function is minimized using the L-BFGS-B algorithm of Byrd et al. (1995) which allows constraining the solution to non-negative values. Evaluating the gradient requires solving the adjoint problem for Eq. (1).

The iteration is continued until a stopping criterion is satisfied, e.g. until the norm of the gradient is reduced by a prescribed factor. However, in Section 4 we will discuss truncating the iteration before formal convergence in order to control the regularization.

Geosci. Model Dev. Discuss., doi:10.5194/gmd-2016-200, 2016
Manuscript under review for journal Geosci. Model Dev.
Published: 15 September 2016

3.2 Assimilation of plume height retrievals

Given the tracer concentration $c(x,y,z)$ in three dimensions, the observation operator for column integrated mass is given by

$$y = m_{ij} = \sum_{k=1}^{N} w_k c(x_i, y_j, z_k) \tag{3}$$

where x_i, y_j and z_k are the gridpoint coordinates and w_k denotes the thickness (in meters) of the *k*th model level. The layer concentrations are often weighted with an averaging kernel (Eskes and Boersma, 2003) to account for the vertically varying sensitivity of the satellite retrieval. In this work, weighting is not applied because the IASI retrievals treat the plume height explicitly.

In the retrievals, the plume height is represented by its centre of mass Z_{CM}. It would be possible to develop an observation operator for Z_{CM}, however, the operator would be nonlinear and only defined for nonzero columns. These problems can be overcome by replacing the centre of mass with the first moment of mass mZ_{CM}. Then, the observations consist of pairs $(m_{ij}, m_{ij}Z_{CM,ij})$ given by

$$\begin{pmatrix} m_{ij} \\ m_{ij}Z_{CM,ij} \end{pmatrix} = \begin{pmatrix} \sum_{k=1}^{N} w_k c_{ijk} \\ \sum_{k=1}^{N} z_k w_k c_{ijk} \end{pmatrix}, \tag{4}$$

where z_k is the height of the *k*th model level and *i* and *j* refer to the horizontal coordinates. Transforming the observations of Z_{CM} into mZ_{CM} changes the magnitudes of observation errors, and introduces a correlation between the observation components m and mZ_{CM}. However, this effect can be evaluated and included into the observation operator.

Denote the means and standard deviations of m and Z_{CM} with μ_m, μ_z and σ_m and σ_z. Assuming that the errors of m and Z_{CM} are normally distributed, it can be shown that the variance of first moment equals

$$\begin{aligned} \mathrm{Var}[mZ_{CM}] = {} & \mu_m^2\sigma_z^2 + \mu_z^2\sigma_m^2 + \sigma_m^2\sigma_z^2 \\ & +2\mu_m\mu_z \mathrm{Cov}[m, Z_{CM}] \\ & +\mathrm{Cov}[m, Z_{CM}]^2. \end{aligned} \tag{5}$$

Under similar assumptions, the covariance of m and mZ_{CM} becomes

$$\mathrm{Cov}[m, mZ_{CM}] = \sigma_m^2\mu_z + \mu_m \mathrm{Cov}[m, Z_{CM}]. \tag{6}$$

Finally, the expectation of mZ_{CM} is shifted due to the correlation between retrievals of m and Z_{CM}:

$$\mathrm{E}[mZ_{CM}] = \mu_m\mu_Z + \mathrm{Cov}[m, Z_{CM}]\ . \tag{7}$$

Geosci. Model Dev. Discuss., doi:10.5194/gmd-2016-200, 2016
Manuscript under review for journal Geosci. Model Dev.
Published: 15 September 2016

The retrieval errors of different pixels are assumed to be uncorrelated. The observation error covariance matrix $\mathbf{R}$ is therefore block-diagonal, and its entries can be evaluated from the known covariances of m and Z_{CM} using Eqs. (5) and (6).

Assimilation schemes commonly assume uncorrelated and unbiased observation errors. A non-diagonal $\mathbf{R}$ can be introduced with a transformation of variables: define

$$\begin{aligned}\mathbf{L}^{\mathrm{T}}\mathbf{L} &= \mathbf{R}^{-1}\\ \tilde{\mathbf{y}} &= \mathbf{L}(\mathbf{y}-\mathbf{b})\\ \tilde{\mathbf{H}} &= \mathbf{L}\mathbf{H}\end{aligned} \tag{8}$$

where $\mathbf{L}^T\mathbf{L}$ is the Cholesky factorisation of the inverse observation error covariance matrix $\mathbf{R}^{-1}$ and $\mathbf{b}=(0,\mathrm{Cov}[m,Z_{CM}])$ corrects for the bias according to Eq. (7). Then, substituting the transformations of Eq. (8) into the cost function (2) shows that assimilation of $\mathbf{y}$ with the original $\mathbf{R}$ is equivalent to assimilation of $\tilde{\mathbf{y}}$ using the transformed observation operator $\tilde{\mathbf{H}}$ with unit matrix in place of $\mathbf{R}$.

The above formulas can be implemented as a preprocessing step for the observations. In summary, the procedure is then as follows:

1. For each available IASI pixel i, evaluate the tuple $\mathbf{y}_i-\mathbf{b}_i=(m_i, m_i Z_{CM,i}-\mathrm{Cov}[m_i, Z_{CM,i}])$ and the corresponding 2x2 covariance matrix $\mathbf{R}_i$.
2. Factorise $\mathbf{R}_i^{-1}=\mathbf{L}_i^T\mathbf{L}_i$ and transform the observations according to Eq. (8).
3. Store the transformed observations $\tilde{\mathbf{y}}_i$ with their pixel-specific vertical weighting functions given by rows of the matrix $\tilde{\mathbf{H}}=\mathbf{L}_i\mathbf{H}$.

After the transformation, the observations are handled identically to regular column observations with a vertical weighting function.

3.3 Observation errors

The IASI retrievals used in this study include pixel-specific error estimates for total column and plume height retrievals. The estimates are derived statistically (Carboni et al., 2012) from differences between the transmission spectra computed by a forward model and those observed by IASI. Together with estimates for the correlation between plume height and total column retrieval errors, this provides the necessary input for equations (5) and (6).

The retrieval error estimates are only provided for pixels with positive SO_2 detection. For the non-SO_2 pixels, which are assimilated as zero values, a different estimate is used, based on the detection limits estimated by Walker et al. (2012). The detection limit was translated into a standard deviation of a Gaussian random variable assuming, conservatively, a probability of 0.95 for a correct detection.

However, performing the inversions with $\mathbf{R}$ defined only by retrieval errors resulted in poor a posteriori agreement with the IASI data, which suggested that the retrieval errors are not sufficient to describe the discrepancy between the simulated and observed values. As found in the synthetic experiments, the impact of model uncertainty is significant compared to the retrieval errors, and it needs to be taken into account. The problem of model errors affecting the inversion is discussed by Boichu et al. (2013), who found the impact to depend strongly on treatment of zero-value observations, and consequently chose to keep only every tenth zero-valued observation.

In this study, the model errors are included by modifying the observation error covariance matrix, which is set to $\mathbf{R} = \mathbf{R}_{obs} + \mathbf{R}_{model}$, where $\mathbf{R}_{model}$ is diagonal and corresponds to experimentally determined constant standard deviations of 2 DU for total column and 1 km for the plume height.

The model errors for plume height and total column are assumed uncorrelated and independent of the observation errors. However, their effect is propagated to the covariance matrix for first moment according to Eq. (5). The actual model errors are likely to be variable and correlated in space and between the plume height and total column components; however, a more advanced treatment appears difficult in the current inversion approach.

3.4 Regularization

The least squares problem (2) has a unique solution only if the matrix $\mathbf{HM}$ is of full (numerical) rank. Furthermore, if $\mathbf{HM}$ is close to singular, the problem remains ill-posed, which results in a noisy solution. Consequently, some form of regularisation has been employed in all previous works based on the least-squares approach.

A common option is the Tikhonov regularisation, which introduces a penalty term into the cost function (2), which in the simplest form becomes

(9) $$J(\mathbf{f}) = \frac{1}{2}(\mathbf{y} - \mathbf{Hx})^T \mathbf{R}^{-1}(\mathbf{y} - \mathbf{Hx}) + \alpha^2 \sum_{k,n} w_k \mid f_{k,n} \mid^2,$$

where the summation is over levels *k* and timesteps *n*. The weights w_k in Eq. (9) are set equal to the thickness of each model layer; this makes the penalty term consistent with its continuous counterpart $\int f(z,t)^2 dtdz$, which in turn ensures that the regularisation term does not depend on the vertical discretisation.

The penalty term can be modified to include a non-zero a priori source term. However, this approach is not taken in the present work. Instead, we aim to choose the level of regularisation optimally, so as to avoid excessive bias in the regularised solution. The need for regularisation depends on the coverage of observations, accuracy of the forward model as well as on the meteorological conditions controlling the dispersion. Thus, the regularisation parameter α^2 cannot be chosen a priori.

In this work, a criterion known as the L-curve (Hansen, 1992) is used for determining the amount of regularisation. In the L-curve approach, the inversion is performed with various values of α^2, and the residual $\|y - Hx\|$ is plotted as a function of the solution norm $\|f\|$. For ill-posed inverse problems, the curve is typically L-shaped. The residual initially reduces quickly as the regularization is relaxed, however, for some value of α^2, the curve flattens and reducing the regularization further only marginally improves the fit. This point, where L-curve reaches its maximum curvature, is taken to represent the optimal regularisation. In the present study, the L-curve is evaluated without the frequently used logarithmic transformation.

The main advantage of the L-curve method is that it does not rely on a priori estimates for the observation error. This is useful, since in practice the discrepancy between simulated observations and the data is also affected by model errors, which are poorly known. The L-curve was, in effect, used in inverse modelling of volcanic SO_2 also by Boichu et al. (2013).

Changing the regularisation parameter requires the minimisation to be started over, which is costly in the variational inversion scheme where each iteration requires a model integration. However, as noted by Fleming (1990) and Santos (1996), the iteration itself forms a sequence of solutions with decreasing regularisation. Thus, instead of minimising the regularised cost function (9), we iterate to minimise the original cost function (2), and truncate the iteration according to the L-curve criterion. In the following section, we show experimentally that such an approach results in similar solutions as the more common Tikhonov regularisation.

4 Experiments with synthetic data

Regularisation by truncated iteration has been studied in detail especially for Krylov subspace based algorithms (Calvetti et al., 2002; Fleming, 1990; Kilmer and O'Leary, 2001). The effect of truncated iteration on quasi-Newton minimisation methods, such as the L-BFGS-B algorithm used in this work, has been studied less extensively. To evaluate the truncated iteration in comparison to Tikhonov regularisation for inverse modelling of volcanic emissions, we performed an experiment with synthetic data generated for the points observed by IASI during the simulated period of 1-21 May, 2010. In addition to the comparison of regularisation methods, the synthetic experiments enable us to evaluate robustness of the L-curve method and to assess how model errors affect the source term estimate.

The inversions were performed for a set of artificial source profiles (cases A to D) shown in the leftmost column of Figure 1. The cases A and B are defined arbitrarily, while cases C and D are realisations of a stochastic process where the total flux (kg/s) is given by a lognormal, temporally correlated random variable and the eruption height follows the relation of Mastin et al. (2009). At each time, a piecewise constant vertical profile is assumed with a transition at 75% of height. The emission rate is distributed evenly between the two sections.

For the sake of computational convenience, the experiments in this section were carried out by pre-evaluating the forward sensitivity matrix **HM** by running a separate model simulation for each component of the emission vector $\mathbf{f}$. In order to simulate the effect of model errors, the matrix **HM** was evaluated with both the ERA-Interim and operational ECMWF forecast fields as meteorological drivers.

The sensitivity matrix for inversions was extracted from the run with ERA-Interim meteorological data. The set of synthetic observations of the SO_2 column density, on the other hand, was evaluated from the model run based on the operational meteorological fields and used as the data for the inversion experiments. The simulated observations were

Geosci. Model Dev. Discuss., doi:10.5194/gmd-2016-200, 2016
Manuscript under review for journal Geosci. Model Dev.
Published: 15 September 2016

perturbed with Gaussian noise with standard deviation equal to 1 DU + 30% of the true value. The observation error covariance matrix used in the inversion was supplemented with 2 DU "model error" as described in Section 3.3.

The residual and solution norms, which define the L-curves, are evaluated consistently to the penalized cost function (9):

$$\|\mathbf{Hx}-\mathbf{y}\| = \sqrt{(\mathbf{Hx}-\mathbf{y})^T \mathbf{R}^{-1} (\mathbf{Hx}-\mathbf{y})} \qquad (10)$$
$$\|\mathbf{f}\| = \sqrt{\sum_{k,n} w_k \mid f_{k,n} \mid^2},$$

where $\mathbf{f}$ denotes the emission, $\mathbf{x}=\mathbf{Mf}$ and w_k is the thickness of the kth model layer. To evaluate the L-curve for Tikhonov-regularisation, the parameter α^2 was incremented in discrete steps given by $\alpha_i^2 = 10^7 \cdot 2^{-i}$ for $i = 0,1,2,\ldots$. The L-BFGS-B minimization method with non-negativity constraint was used for both Tikhonov regularisation and the truncated iteration; in the case of Tikhonov regularisation, the iteration was continued until convergence for each α_i^2. With truncated iteration, the weights w_k, required by Eqs. (9) and (10), are not explicitly included in the cost function. Instead, the same effect is achieved by transforming the parameter vector as $f'_{k,n} = w_k^{1/2} f_{k,n}$.

The point where the L-curve flattens, which is taken as the final solution, was determined numerically. First, the points $(\|\mathbf{f}\|, \|\mathbf{Hx}-\mathbf{y}\|)$ are sorted according to increasing $\|\mathbf{f}\|$. Then, the points where the residual increases are removed, and finally, the optimal point is chosen using the "triangle" algorithm of Castellanos et al. (2002).

The inversion results using truncated iteration and Tikhonov regularisation are presented in the middle and left columns of Figure 1. In each test case, the emission timing is well captured within the 12 h resolution. The overall vertical profiles are also recovered, however, spurious features are present especially in cases B and C. The total emitted mass is underestimated by < 10 % for the solution from truncated and by up to about 15 % for the Tikhonov-regularised solution. The underestimation is expected due to the form of cost function (9). However, the inversion results show that the negative bias is not necessarily large unless the problem is regularised too strongly.

For comparison, Figure 2 presents the solution corresponding to the case B in Figure 1 but evaluated without model errors - that is, using the same sensitivity matrix $\mathbf{HM}$ for both evaluating the observations and performing the inversion. In this case, regularisation was not needed, and the true solution was recovered almost perfectly despite the noisy observations. Thus, the noise present in the estimated solutions in Figure 1 is mainly due to model error, which affects the elements of matrix $\mathbf{M}$.

The L-curves corresponding to each case in Figure 1 are shown in Figs. 3 and 4. The root mean squared error (RMSE) of the solution is shown next to each L-curve as a function of the regularisation parameter. When measured by the solution RMSE, an optimal regularisation indeed existed in each case. In case A, where the solution varies smoothly in time and space, the solution error is only moderately sensitive to the regularisation. The L-curve formed by the L-BFGS-B iterates is shallow in this case, which caused the algorithm to choose an unnecessarily high number of iterations. However, the

Geosci. Model Dev. Discuss., doi:10.5194/gmd-2016-200, 2016
Manuscript under review for journal Geosci. Model Dev.
Published: 15 September 2016

negative effect on the solution quality was small. For the Tikhonov regularisation, the regularisation parameter was determined almost optimally.

The choice of regularisation was more critical in the remaining cases. In cases B and C, the L-curve has a clear plateau after initial decrease, and the chosen corner point is close to optimal for the both regularisation methods. In case D, the truncated iteration leads to a somewhat under-regularised solution similar to case A.

Outcome of the four experiments indicates that the need for regularisation varies strongly depending on the true source, whose characteristics also affect how accurately the algorithm determines the optimal regularisation. We used the stochastic source terms to evaluate this more quantitatively. Figure 5 presents the RMSE as a function of the iteration number for 40 realisations of the stochastic source term used in cases C and D. The optimal iteration numbers chosen from each L-curve are marked with stars.

The RMS errors shown in Figure 5 are normalised by the minimum error for each inversion, which shows that in most cases, the inversion was only moderately sensitive to the exact point of truncation. In 34 cases out of 40, the RMSE of the solution determined from the L-curve was within 20% from the optimally regularised solution. Of the remaining six cases, two were over-regularised and four were under-regularised.

While the experiments in this section were performed by pre-evaluating the matrix $\mathbf{HM}$, in 4D-Var, the multiplications by $\mathbf{HM}$ and its transpose are replaced by forward and adjoint model evaluations. Although the approaches are formally equivalent, this change results in a slightly different sequence of iterations from which the L-curve is evaluated. To investigate this difference, we performed the inversion using the real IASI data using both approaches. The two solutions are shown in Figure 6. The total released mass differs by less than 1% between the solutions, and the emission patterns are qualitatively similar. The differences for individual values, although larger, appear small compared to the inversion errors.

In summary, the experiment with synthetic data showed that the truncated iteration resulted in solutions similar to those obtained with the more common Tikhonov regularisation. This makes the truncated iteration, in combination with the L-curve, an attractive option for regularising the variational source term inversion. On the other hand, the overall need for regularisation depended strongly on the assumed source term. No regularisation was needed in absence of model error, which indicates that the need for regularisation is likely to also depend on quality of the forward model. This emphasizes the need for a robust method to determine the appropriate regularisation according to the situation at hand.

5 Inversion results for Eyjafjallajökull

Optimising the source term following the regularisation strategy described in Section 3.4 results in satellite-derived estimates on the temporal and vertical emission profiles, as well as on the total emitted amount. The solutions presented here correspond to iterates chosen from the L-curve as described in Section 3.4. For assimilation of column mass only, the 9th iterate was chosen; with column mass and plume height assimilation, the 13th iterate was chosen.

Figure 7 shows the temporal and vertical distribution of the SO_2 emission obtained both with and without assimilation of plume height. The plume height time series estimated from radar and camera observations (Petersen et al., 2012) are plotted on top of the emission distributions. Even if the visible plume does not necessarily coincide with the SO_2 plume, the plume height observations provide an indication of the eruption activity.

The strongest emission occurred during 6th May. However, the vertical distribution of the peak depends on whether the plume height is assimilated. While the maximum occurs at 5-6 km, if plume height is not assimilated, secondary maxima appear at 11 km, reaching 13 km on 9th May. If plume height retrievals are assimilated, the emission above about 8 km is strongly suppressed. Similarly, on 18th May, the isolated emissions at 10 and 15 km are essentially removed when the plume height is assimilated.

Figure 8 shows the vertical profile of emissions integrated over the whole period. The bulk of emissions are between 2 and 8 kilometres even if only column density is assimilated. Assimilating the plume height retrievals further decreases the fraction of emissions above 8 km. When the plume height is assimilated, about 85% of total emission is estimated below 8 km and about 95% below 11 km.

The total released mass of SO_2 is 0.33 Tg when plume height is not assimilated and 0.29 Tg when plume height is assimilated. Figure 9 depicts the emission flux as a function of time and shows that while the largest difference in emission rate is during the peaks of 6th May, the assimilation of plume heights tends to decrease the emission rate throughout the eruption.

The inversion results of Figure 7 can be compared with those in Figure 10, which are obtained by assimilating both total column and plume height but neglecting all off-diagonal observation error covariance matrix elements. The distribution of emissions differs strongly from both cases in Figure 7, and the vertical distribution remains as spread as with assimilation of total column only. The treatment of observation errors as described in Section 3.2 is therefore a necessary step for successful assimilation of the plume height retrievals.

The SO_2 column densities simulated a posteriori are shown for 5-10 May in Figs. 11 and 12, along with the corresponding IASI retrievals. The overall patterns are well reproduced, although the column density is underestimated for some parts of the plume, especially on 7th and 8th of May. Due to the smaller total emission, the column densities are slightly lower when plume height is assimilated, however, the difference is small.

The plume height, evaluated as centre of mass, for 6-9 May is shown in Figure 13. Compared to IASI, the simulation based only on assimilation of total columns tends to overestimate the plume height for all four days. When the plume height retrievals are assimilated, the overestimation is reduced consistently, although not entirely removed.

6 Discussion

No a priori assumptions regarding shape the emission profile were made in this study. If only total column retrievals are used in the inversion, the estimated source term includes isolated emissions reaching up to 15 km. With plume height assimilation, the vertical distribution becomes more concentrated and also more consistent with the plume observed with the radar, which suggests that the vertical distribution SO_2 and ash emissions was mostly similar.

The centre of mass retrievals only partly constrain the vertical distribution, and hence some emission remains between 8 and 12 km, and the overestimation of plume height is reduced but not removed in the a posteriori simulations. However, given the about 1 km uncertainty in the IASI plume height retrievals and the 1 km assumed model uncertainty (Section 3.3) included into the observation errors, the inversion results for plume height are consistent with the assumptions of the inversion.

Previous studies based on Lidar observations (Ansmann et al., 2010), aircraft measurements (Schumann et al., 2011) or inverse modelling (Stohl et al., 2011) do not suggest significant injection above the 10 km altitude. However, these studies were focused on volcanic ash instead of SO_2, and as shown by Thomas and Prata (2011) , ash and SO_2 were not always transported together. In contrast, the SO_2 plume height estimates derived from the GOME-2 satellite instrument by Rix et al. (2012) do indicate heights above 10 km and up to 13 km on 5th of May. However, the plume heights retrieved from IASI data are below 6 km for that day, which agrees with the modelled plume heights (not shown) even when only total column retrievals are included in the inversion.

Among the previous emissions estimates for Eyjafjallajökull, Flemming and Inness (2013) estimated a 0.25 Tg total SO_2 release using GOME-2 satellite retrievals, and 0.14 Tg using the OMI retrievals. Our estimates of 0.29-0.33 Tg are higher, especially compared OMI, but this is consistent with the higher total SO_2 burden estimated (Carboni et al., 2012) from the IASI data used in this study.

The experiments with synthetic data (Section 4) show that the need for regularisation, or in Bayesian terms, the need for a priori information, strongly depends on the situation. In addition, the need for regularisation was strongly affected by uncertainty of the forward model, and the efforts needed to handle zero-valued observations in this and other studies support this conclusion. The errors arising from the dispersion model are likely to be correlated in space, and therefore, introducing the corresponding non-diagonal elements in the error covariance matrix $\mathbf{R}$ could improve the inversion results.

The model errors resulted in noisy temporal and vertical emission profiles in the synthetic experiments and probably also in the real inversions. However, the estimates for total emission were fairly robust regardless of the assumed source term or perturbations to the forward model. Also, halving the vertical resolution of the reconstruction (compare Figs. 6 and 7) resulted in only minimal change in the total emission. Nevertheless, the estimates of the total emission could be affected by biases in the satellite retrievals, or by model errors not exposed by the change of meteorological driver.

While the regularisation used in this work is equivalent to a zero-valued a priori source, a more informative a priori source could be accommodated with a change of variables. Other forms of regularisation proposed for the volcanic source term inversion include second-order temporal smoothing (Boichu et al., 2013), which also could be handled by truncated iteration as discussed by Calvetti et al. (2002).

The variational inversion method is computationally efficient if high temporal or vertical resolution is desired for the reconstruction. In the current configuration, the reconstructed solution had formally 1360 degrees of freedom. Each iteration

Geosci. Model Dev. Discuss., doi:10.5194/gmd-2016-200, 2016
Manuscript under review for journal Geosci. Model Dev.
Published: 15 September 2016

consisting of one forward and one adjoint integration, the 25 iterations would require about 1000 days to be simulated. In comparison, evaluating the matrix $\mathbf{HM}$ directly would require 1360 model integrations, and if the sensitivity was evaluated in windows of eg. 72 hours, almost 4000 simulated days would be required.

A drawback of the 4D-Var inversion method is that the a posteriori error covariance matrix for the source term is difficult to evaluate. However, Monte Carlo techniques could be used to sample the a posteriori uncertainty.

7 Conclusions

We have presented an observation operator for retrievals of the vertical centre of mass of a tracer plume. The operator is based on transforming the centre of mass into first moment of mass using the retrieval of total column. The approach was tested by performing a source term inversion using SO_2 retrievals from the IASI instrument during the Eyjafjallajökull eruption in May 2010.

Assimilating the plume height retrievals reduced the vertical spread of the SO_2 injection. When the plume height is assimilated, about 85% of total emission was below 8 km and about 95% was below 11 km. The injection profile obtained by assimilating the plume height retrievals is more consistent with the radar and camera based observations of the ash plume.

The inverse problem was solved with the 4D-Var method embedded into the SILAM dispersion model. Truncated iteration is proposed as an efficient regularisation method for the 4D-Var inversion. Using both real and synthetic data, the 4D-Var method was shown to produce a similar solution as the more common algebraic method, but at considerably lower computational cost.

Experiments with both synthetic and real data suggest that the inversion is sensitive to errors in the forward model, and to their assumed uncertainty. Methods more robust to model errors are a topic suitable for future research.

Appendix: moments of products of correlated Gaussian random variables

Let X and Y be scalar random variables with means and variances μ_X, μ_Y, σ_X^2 and σ_Y^2. Then, it follows from the definitions for variance and covariance that

(11) $$\mathrm{Var[XY]} = \sigma_X^2\sigma_Y^2 + \mu_X^2\sigma_Y^2 + \mu_Y^2\sigma_X^2 - 2\mu_X\mu_Y\mathrm{Cov}[X,Y] - \mathrm{Cov}[X,Y]^2 + \mathrm{Cov}[X^2,Y^2]$$

and

(12) $$\mathrm{Cov[X,XY]} = \mathrm{E[X^2]}E[Y] + \mathrm{Cov}[X^2,Y] - \mathrm{E}[X]\mathrm{E}[XY] \ .$$

To expand $\mathrm{Cov}[X^2,Y^2]$ and $\mathrm{Cov}[X^2,Y]$ we assume that X and Y are normally distributed. We first define normalized auxiliary variables

(13) $$\tilde{X} = \frac{X-\mu_X}{\sigma_x}, \tilde{Y} = \frac{Y-\mu_Y}{\sigma_Y} \ .$$

Geosci. Model Dev. Discuss., doi:10.5194/gmd-2016-200, 2016
Manuscript under review for journal Geosci. Model Dev.
Published: 15 September 2016

Geoscientific Model Development Discussions
Open Access

Then, by expressing $\tilde{Y}$ as

$$\tilde{Y} = c\tilde{X} + \sqrt{1-c^2}\,\tilde{Z}\ , \tag{14}$$

where $c = \mathrm{Cov}[\tilde{X},\tilde{Y}]$ and $\tilde{Z} \sim \mathcal{N}(0,1)$ independent of $\tilde{X}$, it is simple to verify that

$$\begin{aligned}&\mathrm{Cov}[\tilde{X}^2,\tilde{Y}^2] = 2c^2\\ &\mathrm{Cov}[\tilde{X}^2,\tilde{Y}] = 0.\end{aligned} \tag{15}$$

For the original random variables X and Y, we find by substituting (13) into the definition, expanding the terms, and using identities (15) that

$$\mathrm{Cov}[\mathrm{X}^2,Y^2] = 2\mathrm{Cov}[X,Y]^2 + 4\mu_X\mu_Y\mathrm{Cov}[X,Y] \tag{16}$$

and

$$\mathrm{Cov}[X^2,Y] = 2\mu_X\mathrm{Cov}[X,Y]\ . \tag{17}$$

Formulas (5) and (6) now follow by combining Eqs. (16) and (17) with (11) and (12).

Code availability

The source code for SILAM v5.3, including the data assimilation component, is available on request from the authors (julius.vira@fmi.fi, mikhail.sofiev@fmi.fi).

Acknowledgements

This work has been supported by the ESA projects SMASH and VAST and Nordforsk Centre of Excellence EmblA. E.C and R.G.G. acknowledge funding from the NERC SHIVA (NE/J023310/1) and VANAHEIM (NE/1015592/1) projects. The work of E.C. has been partly funded by the EC-FP7 APhoRISM project. The authors thank Marje Prank for comments on the manuscript.

References

Ansmann, A., Tesche, M., Groß, S., Freudenthaler, V., Seifert, P., Hiebsch, A., Schmidt, J., Wandinger, U., Mattis, I., Müller, D., Wiegner, M., 2010. The 16 April 2010 major volcanic ash plume over central Europe: EARLINET lidar and AERONET photometer observations at Leipzig and Munich, Germany. Geophys. Res. Lett. 37, 1–5. doi:10.1029/2010GL043809

Bernard, A., Rose, W.I., 1990. The injection of sulfuric acid aerosols in the stratosphere by the El Chichón volcano and its related hazards to the international air traffic. Nat. Hazards 3, 59–67. doi:10.1007/BF00144974

Boichu, M., Clarisse, L., 2014. Improving volcanic sulfur dioxide cloud dispersal forecasts by progressive assimilation of satellite observations. Geophys. … 41, 2637–2643. doi:10.1002/2014GL059496.Abstract

Boichu, M., Menut, L., Khvorostyanov, D., Clarisse, L., Clerbaux, C., Turquety, S., Coheur, P.-F., 2013. Inverting for volcanic SO 2 flux at high temporal resolution using spaceborne plume imagery and chemistry-transport modelling: the 2010 Eyjafjallajökull eruption case study. Atmos. Chem. Phys. 13, 8569–8584. doi:10.5194/acp-13-8569-2013

Byrd, R.H., Lu, P., Nocedal, J., Zhu, C., 1995. A limited memory algorithm for bound constrained optimization. SIAM J. Sci. Comput. 16, 1190–1208.

Calvetti, D., Lewis, B., Reichel, L., 2002. GMRES, L-curves, and discrete ill-posed problems. BIT Numer. Math. xx, 1–22.

Carboni, E., Grainger, R., Walker, J., Dudhia, a., Siddans, R., 2012. A new scheme for sulphur dioxide retrieval from IASI measurements: application to the Eyjafjallajökull eruption of April and May 2010. Atmos. Chem. Phys. 12, 11417–11434. doi:10.5194/acp-12-11417-2012

Carboni, E., Grainger, R.G., Mather, T.A., Pyle, D.M., Thomas, G., Siddans, R., Smith, A., Dudhia, A., Koukouli, M.L., Balis, D., 2016. The vertical distribution of volcanic SO2 plumes measured by IASI. Atmos. Chem. Phys. 16, 4343–4367. doi:doi:10.5194/acp-16-4343-2016

Carn, S.A., Krueger, A.J., Krotkov, N.A., Yang, K., Evans, K., 2009. Tracking volcanic sulfur dioxide clouds for aviation hazard mitigation. Nat. Hazards 51, 325–343. doi:10.1007/s11069-008-9228-4

Castellanos, J.L., Gómez, S., Guerra, V., 2002. The triangle method for finding the corner of the L-curve ☆. Appl. Numer. Math. 43, 359–373.

Dacre, H.F., Grant, A.L.M., Harvey, N.J., Thomson, D.J., Webster, H.N., Marenco, F., 2014. Volcanic ash layer depth: Processes and mechanisms. Geophys. Res. Lett. 42. doi:10.1002/2014GL062454

Dee, D.P., Uppala, S.M., Simmons, a. J., Berrisford, P., Poli, P., Kobayashi, S., Andrae, U., Balmaseda, M. a., Balsamo, G., Bauer, P., Bechtold, P., Beljaars, a. C.M., van de Berg, L., Bidlot, J., Bormann, N., Delsol, C., Dragani, R., Fuentes, M., Geer, a. J., Haimberger, L., Healy, S.B., Hersbach, H., Hólm, E. V., Isaksen, L., Kållberg, P., Köhler, M., Matricardi, M., McNally, a. P., Monge-Sanz, B.M., Morcrette, J.-J., Park, B.-K., Peubey, C., de Rosnay, P., Tavolato, C., Thépaut, J.-N., Vitart, F., 2011. The ERA-Interim reanalysis: configuration and performance of the data assimilation system. Q. J. R. Meteorol. Soc. 137, 553–597. doi:10.1002/qj.828

Eckhardt, S., Prata, A.J., Seibert, P., Stebel, K., Stohl, A., 2008. Estimation of the vertical profile of sulfur dioxide injection into the atmosphere by a volcanic eruption using satellite column measurements and inverse transport modeling. Atmos. Chem. Phys. 8, 3881–3897. doi:10.5194/acpd-8-3761-2008

Elbern, H., Schmidt, H., Talagrand, O., Ebel, a., 2000. 4D-variational data assimilation with an adjoint air quality model for emission analysis. Environ. Model. Softw. 15, 539–548. doi:10.1016/S1364-8152(00)00049-9

Eskes, H.J., Boersma, K.F., 2003. Averaging kernels for DOAS total-column satellite retrievals. Atmos. Chem. Phys. 3, 1285–1291.

Fleming, H.E., 1990. Equivalence of regularization and truncated iteration in the solution of III-posed image reconstruction problems. Linear Algebra Appl. 130, 133–150. doi:10.1016/0024-3795(90)90210-4

Flemming, J., Inness, A., 2013. Volcanic sulfur dioxide plume forecasts based on UV-satellite retrievals for the 2011 Grímsvötn and the 2010 Eyjafjallajökull eruption. J. Geophys. Res. Atmos. 118. doi:10.1002/jgrd.50753

Fromm, M., Kablick, G., Nedoluha, G., Carboni, E., Grainger, R., Campbell, J., Lewis, J., 2014. Correcting the record of volcanic stratospheric aerosol impact: Nabro and Sarychev Peak. J. Geophys. Res. Atmos. 119, 10,343–10,364. doi:10.1002/2014JD021507

Gudmundsson, M.T., Thordarson, T., Höskuldsson, A., Larsen, G., Björnsson, H., Prata, F.J., Oddsson, B., Magnússon, E., Högnadóttir, T., Petersen, G.N., Hayward, C.L., Stevenson, J. a, Jónsdóttir, I., 2012. Ash generation and distribution from the April-May 2010 eruption of Eyjafjallajökull, Iceland. Sci. Rep. 2. doi:10.1038/srep00572

Hansen, P.C., 1992. Analysis of Discrete Ill-Posed Problems by Means of the L-Curve. SIAM Rev. 34, 561–580. doi:10.1137/1034115

Kilmer, M.E., O'Leary., D.P., 2001. Choosing Regularization Parameters in Iterative Methods for Ill-Posed Problems. SIAM J. Matrix Anal. Appl. 22, 1204–1221. doi:10.1137/S0895479899345960

Koukouli, M.E., Clarisse, L., Carboni, E., van Gent, J., Spinetti, C., Balis, D., Dimopuolos, S., Grainger, R., Theys, N., Tampellini, L., Zehner, C., 2014. Intercomparison of Metop-A SO2 measurements during the 2010-2011 Icelandic eruptions. Ann. Geophys. Fast Track. doi:10.4401/ag-6613

Kristiansen, N.I., Stohl, A., Prata, A.J., Richter, A., Eckhardt, S., Seibert, P., Hoffmann, A., Ritter, C., Bitar, L., Duck, T.J., Stebel, K., 2010. Remote sensing and inverse transport modeling of the Kasatochi eruption sulfur dioxide cloud. J. Geophys. Res. 115, 1–18. doi:10.1029/2009JD013286

Le Dimet, F.-X., Talagrand, O., 1986. Variational algorithms for analysis and assimilation of meteorological observations: theoretical aspects. Tellus A 38A, 97–110. doi:10.1111/j.1600-0870.1986.tb00459.x

Lu, S., Lin, H.X., Heemink, A.W., Fu, G., Segers, A.J., 2016. Estimation of Volcanic Ash Emissions Using Trajectory-Based 4D-Var Data Assimilation. Mon. Weather Rev. 144, 575–589. doi:10.1175/MWR-D-15-0194.1

Mastin, L.G., Guffanti, M., Servranckx, R., Webley, P., Barsotti, S., Dean, K., Durant, a., Ewert, J.W., Neri, a., Rose, W.I., 2009. A multidisciplinary effort to assign realistic source parameters to models of volcanic ash-cloud transport and dispersion during eruptions. J. Volcanol. Geotherm. Res. 186, 10–21. doi:10.1016/j.jvolgeores.2009.01.008

Petersen, G.N., Bjornsson, H., Arason, P., von Löwis, S., 2012. Two weather radar time series of the altitude of the volcanic plume during the May 2011 eruption of Grímsvötn, Iceland. Earth Syst. Sci. Data 4, 121–127. doi:10.5194/essdd-5-281-2012

Rix, M., Valks, P., Hao, N., Loyola, D., Schlager, H., Huntrieser, H., Flemming, J., Koehler, U., Schumann, U., Inness, A., 2012. Volcanic SO2 , BrO and plume height estimations using GOME-2 satellite measurements during the eruption of Eyjafjallajökull in May 2010. J. Geophys. Res. Atmos. 117. doi:10.1029/2011JD016718

Robock, A., 2000. Volcanic eruptions and climate. Rev. Geophys. 38, 191–219.

Santos, R.J., 1996. Equivalence of regularization and truncated iteration for general ill-posed problems. Linear Algebra Appl. 236, 25–33.

Schmidt, A., Leadbetter, S., Theys, N., Carboni, E., Witham, C.S., Stevenson, J.A., Birch, C.E., Thordarson, T., Turnock, S., Barsotti, S., Delaney, L., Feng, W., Grainger, R.G., Hort, M.C., Höskuldsson, Á., 2015. Satellite detection, long-range transport and air quality impacts of sulfur dioxide from the 2014-2015 flood lava eruption at Bárðarbunga (Iceland). J. Geophys. Res. Atmos. 120, 9739–9757. doi:10.1002/2015JD023638.Received

Schumann, U., Weinzierl, B., Reitebuch, O., Schlager, H., Minikin, a., Forster, C., Baumann, R., Sailer, T., Graf, K., Mannstein, H., Voigt, C., Rahm, S., Simmet, R., Scheibe, M., Lichtenstern, M., Stock, P., Rüba, H., Schäuble, D., Tafferner, a., Rautenhaus, M., Gerz, T., Ziereis, H., Krautstrunk, M., Mallaun, C., Gayet, J.-F., Lieke, K., Kandler, K., Ebert, M., Weinbruch, S., Stohl, a., Gasteiger, J., Groß, S., Freudenthaler, V., Wiegner, M., Ansmann, a., Tesche, M., Olafsson, H., Sturm, K., 2011. Airborne observations of the Eyjafjalla volcano ash cloud over Europe during air space closure in April and May 2010. Atmos. Chem. Phys. 11, 2245–2279. doi:10.5194/acp-11-2245-2011

Sofiev, M., 2000. A model for the evaluation of long-term airborne pollution transport at regional and continental scales. Atmos. Environ. 34, 2481–2493. doi:10.1016/S1352-2310(99)00415-X

Sofiev, M., Vira, J., Kouznetsov, R., Prank, M., Soares, J., Genikhovich, E., 2015. Construction of an Eulerian atmospheric dispersion model based on the advection algorithm of M . Galperin : dynamic cores. Geosci. Model Dev. Discuss. 8, 2905–2947. doi:10.5194/gmdd-8-2905-2015

Geosci. Model Dev. Discuss., doi:10.5194/gmd-2016-200, 2016
Manuscript under review for journal Geosci. Model Dev.
Published: 15 September 2016

Spinetti, C., Salerno, G.G., Caltabiano, T., Carboni, E., Clarisse, L., Corradini, S., Grainger, R.G., Hedelt, P.A., Koukouli, M.E., Merucci, L., Siddans, R., Tampellini, L., Theys, N., Valks, P., Zehner, C., 2014. Volcanic SO2 by UV-TIR satellite retrievals: validation by using ground-based network at Mt. Etna. Ann. Geophys. Fast Track. doi:10.4401/ag-6641

Spivakovsky, C.M., Logan, J.A., Montzka, S.A., Balkanski, Y.J., Foreman-Fowler, M., Jones, D.B.A., Horowitz, L.W., Fusco, A.C., Brenninkmeijer, C.A.M., Prather, M.J., Wofsy, S.C., McElroy, M.B., 2000. Three-dimensional climatological distribution of tropospheric OH: Update and evaluation. J. Geophys. Res. 105, 8931–8980.

Stohl, A., Prata, A.J., Eckhardt, S., Clarisse, L., Durant, A., Henne, S., Kristiansen, N.I., Minikin, A., Schumann, U., Seibert, P., Stebel, K., Thomas, H.E., Thorsteinsson, T., Tørseth, K., Weinzierl, B., 2011. Determination of time- and height-resolved volcanic ash emissions and their use for quantitative ash dispersion modeling: the 2010 Eyjafjallajökull eruption. Atmos. Chem. Phys. 11, 4333–4351. doi:10.5194/acp-11-4333-2011

Theys, N., Campion, R., Clarisse, L., Brenot, H., van Gent, J., Dils, B., Corradini, S., Merucci, L., Coheur, P.-F., Van Roozendael, M., Hurtmans, D., Clerbaux, C., Tait, S., Ferrucci, F., 2013. Volcanic SO2 fluxes derived from satellite data : a survey using OMI , GOME-2 , IASI and MODIS. Atmos. Chem. Phys. 13, 5945–5968. doi:10.5194/acp-13-5945-2013

Thomas, H.E., Prata, A.J., 2011. Sulphur dioxide as a volcanic ash proxy during the April–May 2010 eruption of Eyjafjallajökull Volcano, Iceland. Atmos. Chem. Phys. 11, 6871–6880. doi:10.5194/acp-11-6871-2011

Walker, J.C., Carboni, E., Dudhia, a, Grainger, R.G., 2012. Improved detection of sulphur dioxide in volcanic plumes using satellite-based hyperspectral infrared measurements: Application to the Eyjafjallajökull 2010 eruption. J. Geophys. Res. Atmos. 117, n/a–n/a. doi:10.1029/2011JD016810

Wang, J., Park, S., Zeng, J., Ge, C., Yang, K., Carn, S., Krotkov, N., Omar, a. H., 2013. Modeling of 2008 Kasatochi volcanic sulfate direct radiative forcing: assimilation of OMI SO_2 plume height data and comparison with MODIS and CALIOP observations. Atmos. Chem. Phys. 13, 1895–1912. doi:10.5194/acp-13-1895-2013

Wilkins, K.L., Watson, I.M., Kristiansen, N.I., Webster, H.N., Thomson, D.J., Dacre, H.F., Prata, A.J., 2015. Using data insertion with the NAME model to simulate the 8 May 2010 Eyjafjallajökull volcanic ash cloud. J. Geophys. Res. Atmos. 121. doi:10.1002/2015JD023895

Vira, J., Sofiev, M., 2012. On variational data assimilation for estimating the model initial conditions and emission fluxes for short-term forecasting of SOx concentrations. Atmos. Environ. 46, 318–328. doi:10.1016/j.atmosenv.2011.09.066

Zehner, C. (Ed.), 2012. Monitoring volcanic ash from space. ESA-EUMETSAT workshop on the 14 April to 23 May 2010 eruption at the Eyjafjöll volcano, South Iceland (ESA/ESRIN, 26-27 May 2010). ESA Publication STM-280.

Geosci. Model Dev. Discuss., doi:10.5194/gmd-2016-200, 2016
Manuscript under review for journal Geosci. Model Dev.
Published: 15 September 2016

Geoscientific Model Development Discussions
Open Access

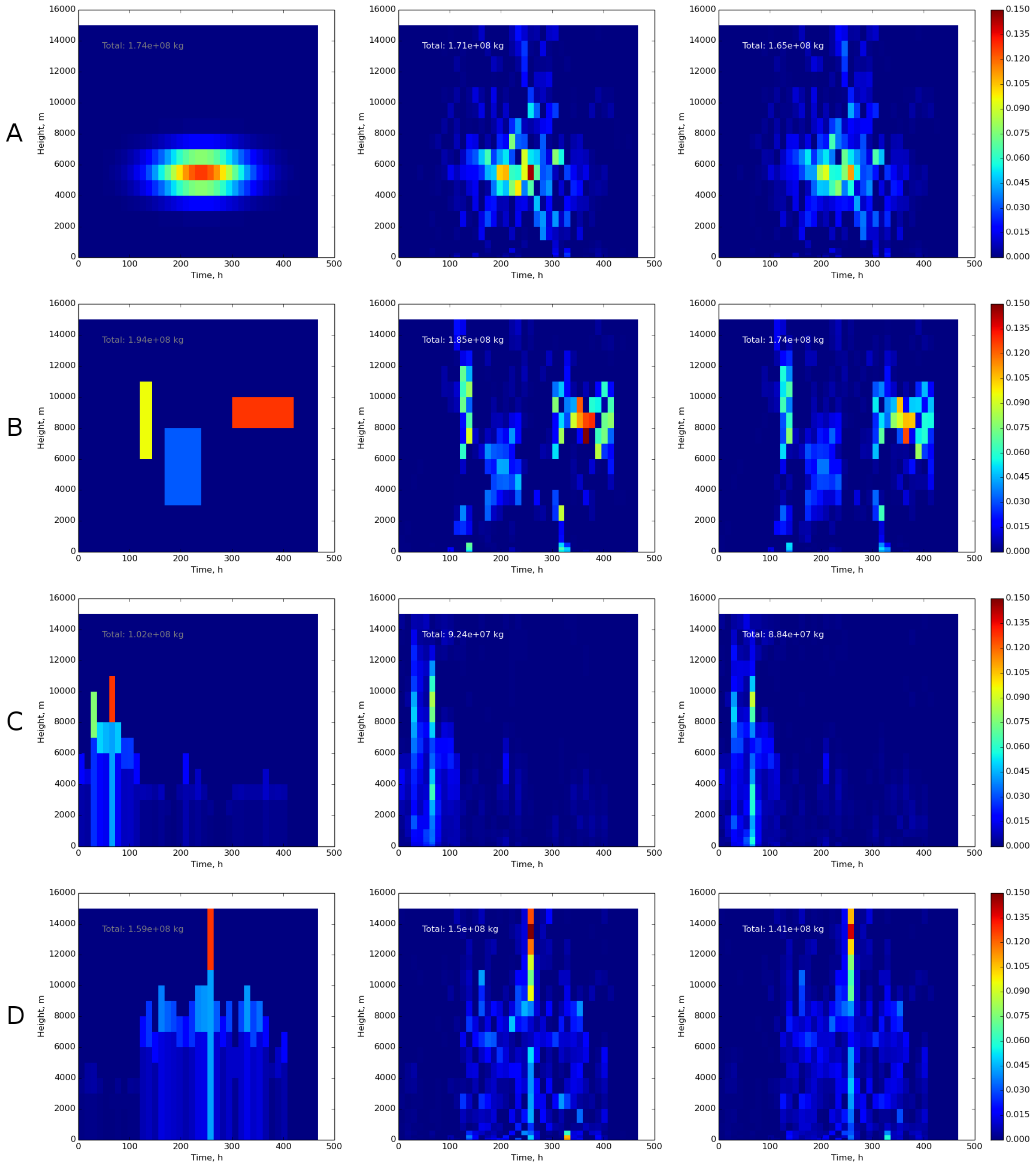

Figure 1. Estimated emission flux (kg m^{-1} s^{-1}) in source term inversions with simulated data. True source terms for the four cases (A to D) are shown in the left column. Solutions using truncated iteration are shown in the middle column, solutions using Tikhonov regularisation are shown in the right column.

Geosci. Model Dev. Discuss., doi:10.5194/gmd-2016-200, 2016
Manuscript under review for journal Geosci. Model Dev.
Published: 15 September 2016

Geoscientific Model Development Discussions
Open Access

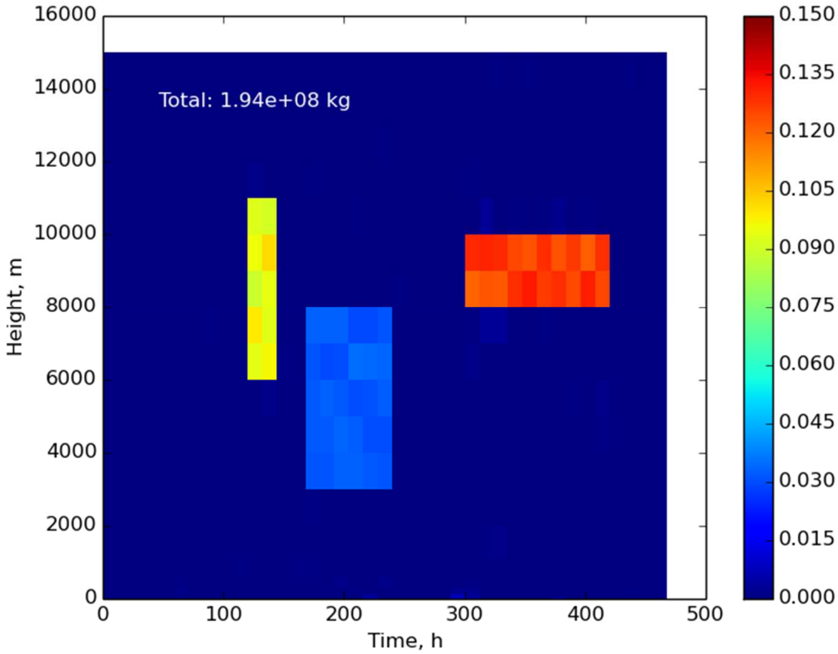

564
565 **Figure 2. Estimated emission flux with synthetic data: inversion results for the case B in Figure 1 assuming a perfect forward**
566 **model.**

Geosci. Model Dev. Discuss., doi:10.5194/gmd-2016-200, 2016
Manuscript under review for journal Geosci. Model Dev.
Published: 15 September 2016

Geoscientific Model Development Discussions
Open Access

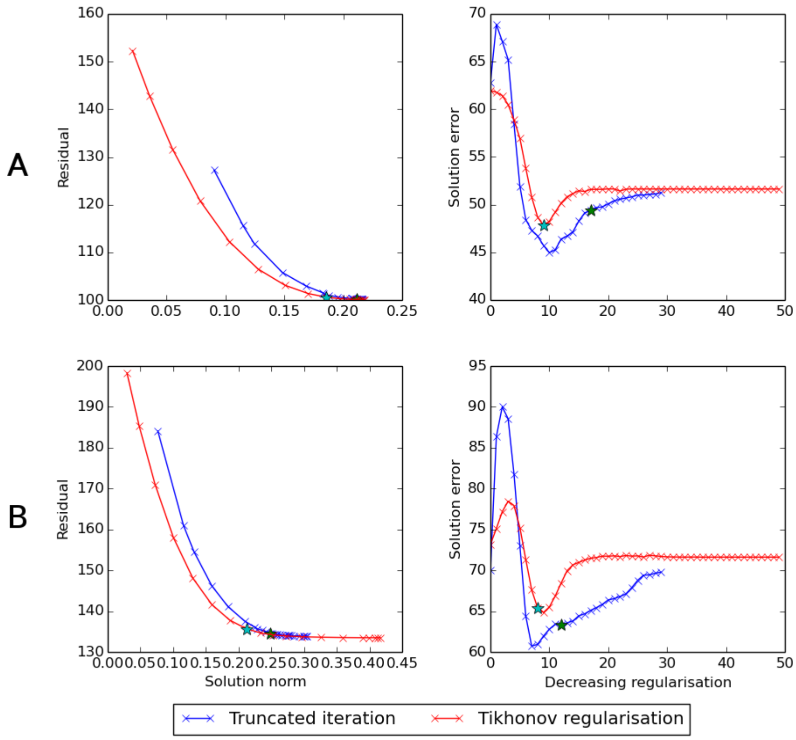

Figure 3. L-curve (left) and RMS error (right) for inversions with simulated data for cases A and B in Figure 1. The iterate (for truncated iteration) or regularisation parameter (for Tikhonov regularisation) chosen from the L-curve is marked with a star.

Geosci. Model Dev. Discuss., doi:10.5194/gmd-2016-200, 2016
Manuscript under review for journal Geosci. Model Dev.
Published: 15 September 2016

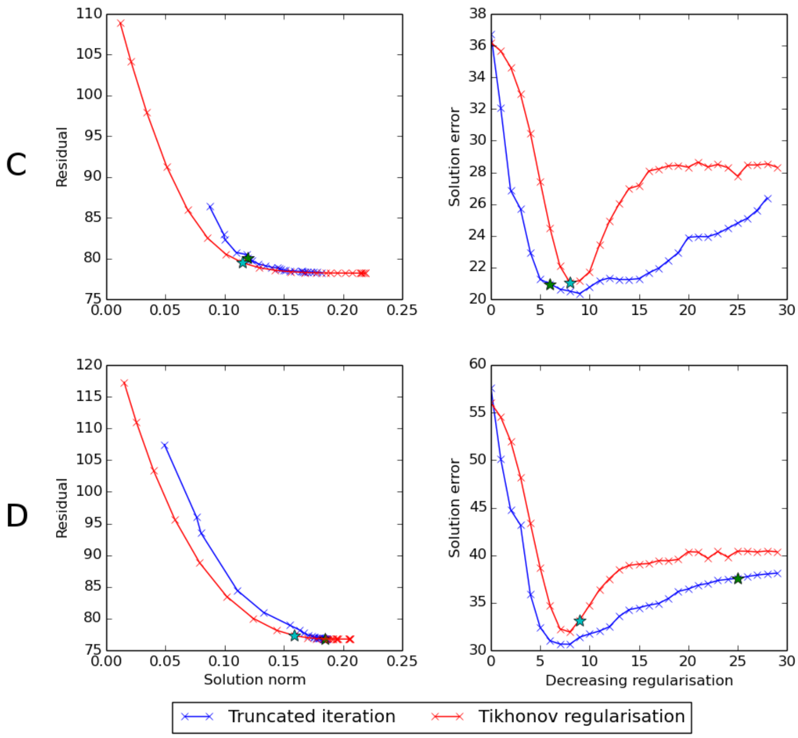

Figure 4. L-curve (left) and RMS error (right) for inversions with simulated data for cases C and D in Figure 1. The iterate (for truncated iteration) or regularisation parameter (for Tikhonov regularisation) chosen from the L-curve is marked with a star.

Geosci. Model Dev. Discuss., doi:10.5194/gmd-2016-200, 2016
Manuscript under review for journal Geosci. Model Dev.
Published: 15 September 2016

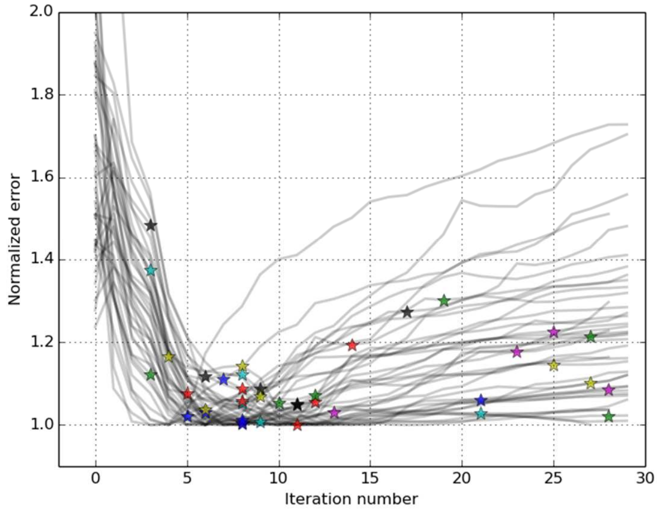

574

575 **Figure 5. The normalised RMSE with respect to iteration number. Each grey line corresponds to an inversion with a randomly**
576 **generated source term. The colourful stars denote solutions chosen from the L-curve.**

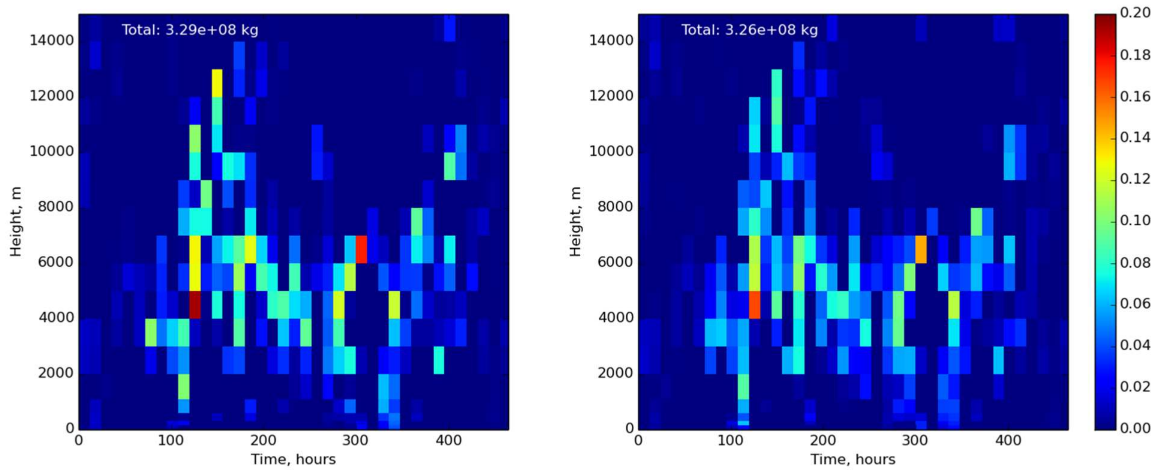

577 **Figure 6. Inversion results with real observations: emission flux (kg m^{-1} s^{-1}) obtained using 4D-Var (left) and by evaluating the**
578 **sensitivity matrix (right).**

Geosci. Model Dev. Discuss., doi:10.5194/gmd-2016-200, 2016
Manuscript under review for journal Geosci. Model Dev.
Published: 15 September 2016

Geoscientific Model Development Discussions
Open Access

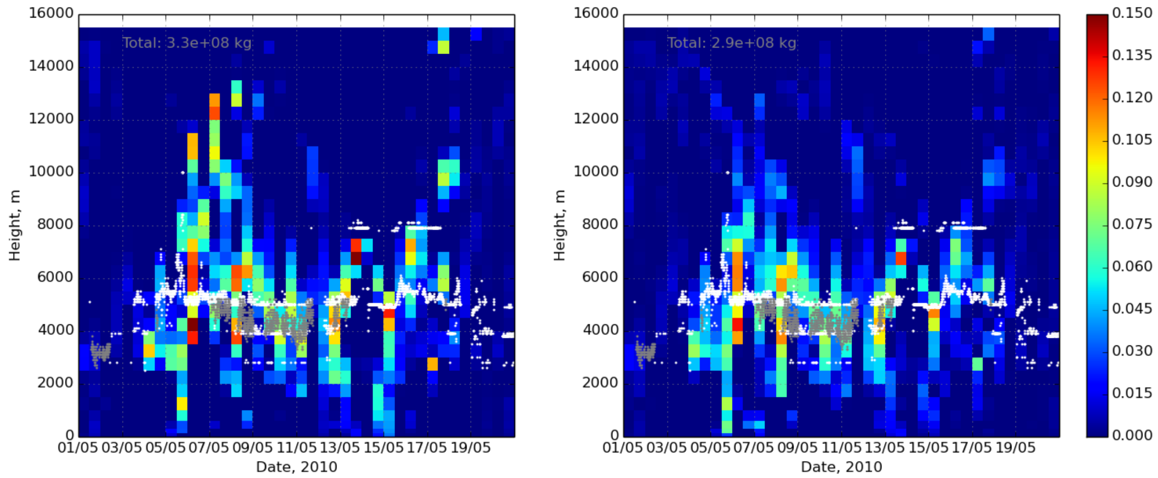

Figure 7. Inversion results for Eyjafjallajökull. Left: emission flux (kg m^{-1} s^{-1}) with assimilation of column mass only. Right: assimilation of column mass and plume height with full observation error covariance matrix. White dots denote plume height observations by radar, grey dots denote plume height observations with a camera.

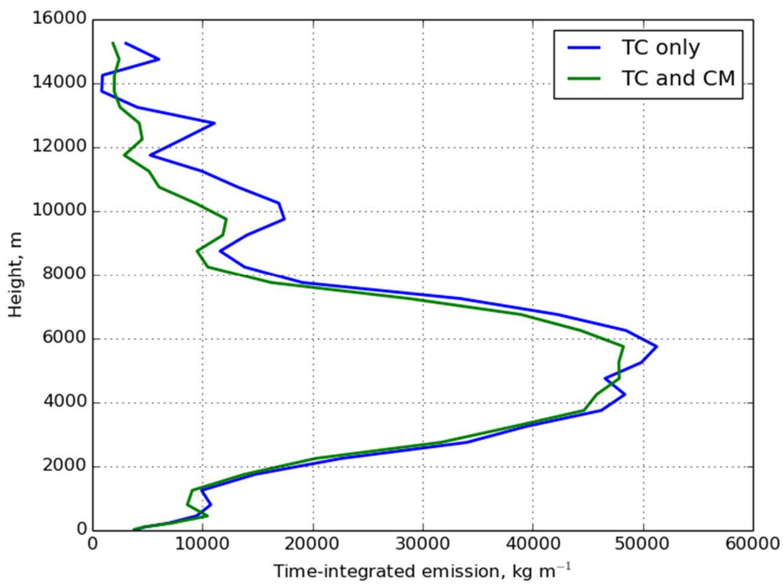

Figure 8. Time-integrated emission of SO_2 (kg m^{-1}) during the simulated period as function of height (m) for the source term inversions with (green) and without (blue) plume height assimilation.

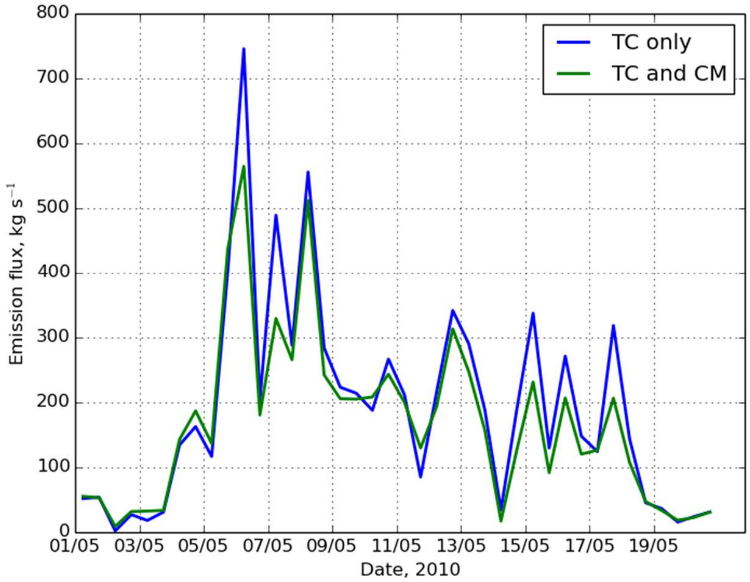

Figure 9. Estimated SO_2 emission flux (kg s^{-1}) as function of time with (green) and without (blue) assimilation of plume height retrievals.

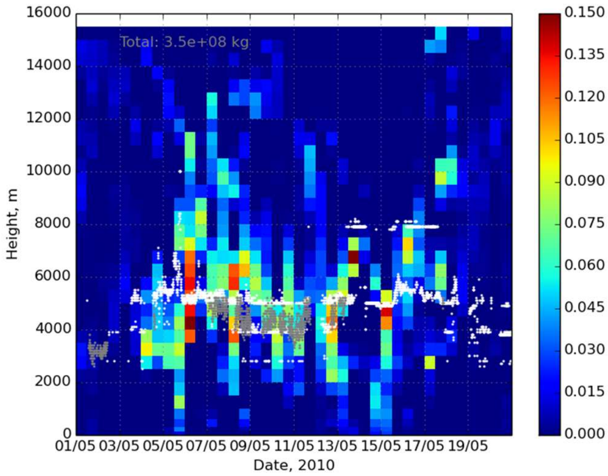

Figure 10. Inversion results for Eyjafjallajökull: emission flux (kg m^{-1} s^{-1}) with assimilation of column density and plume height but neglecting off-diagonal elements in the observation error covariance matrix. White dots denote plume height observations by radar, grey dots denote plume height observations with a camera.

Geosci. Model Dev. Discuss., doi:10.5194/gmd-2016-200, 2016
Manuscript under review for journal Geosci. Model Dev.
Published: 15 September 2016

Geoscientific Model Development Discussions
Open Access

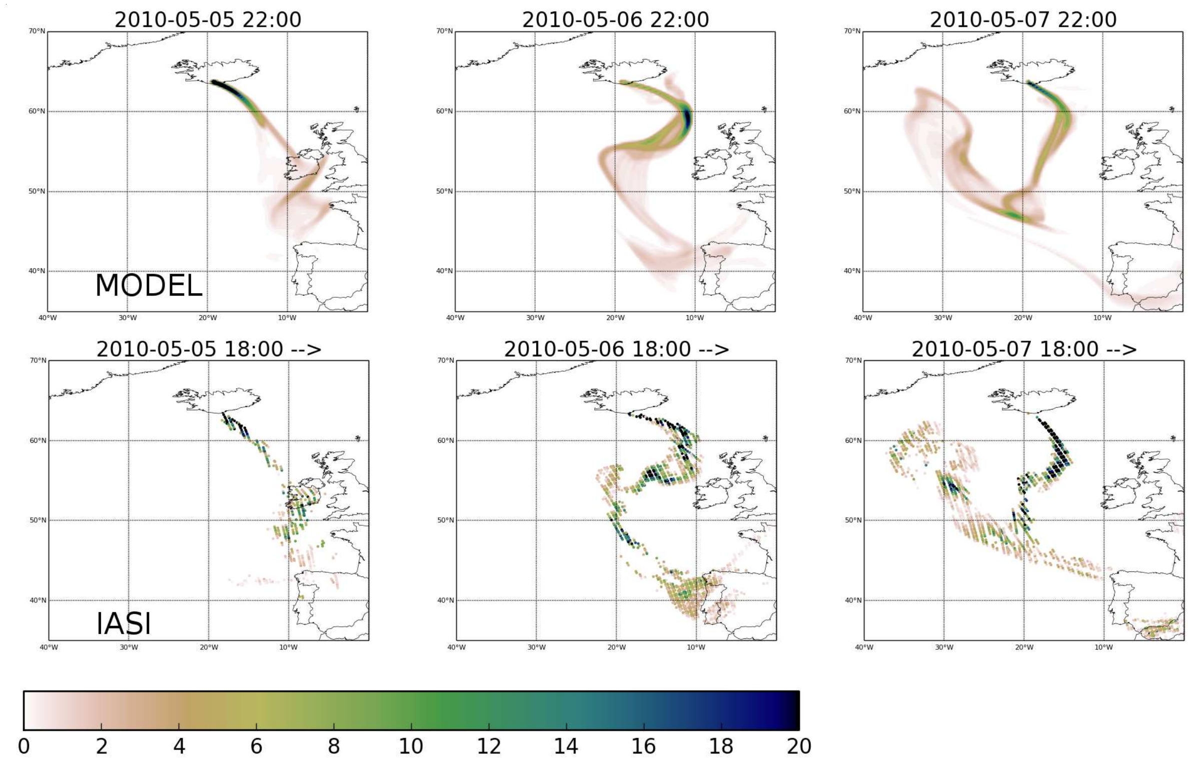

595
596 **Figure 11. SO_2 column loading (DU) for the a posteriori simulation with assimilation of plume height (top) and for the IASI**
597 **column retrievals (bottom row). Results for 5, 6 and 7th May, 2010 are shown in the columns from left to right. The evening**
598 **overpasses are shown for IASI, the model fields are valid at 22 UTC.**

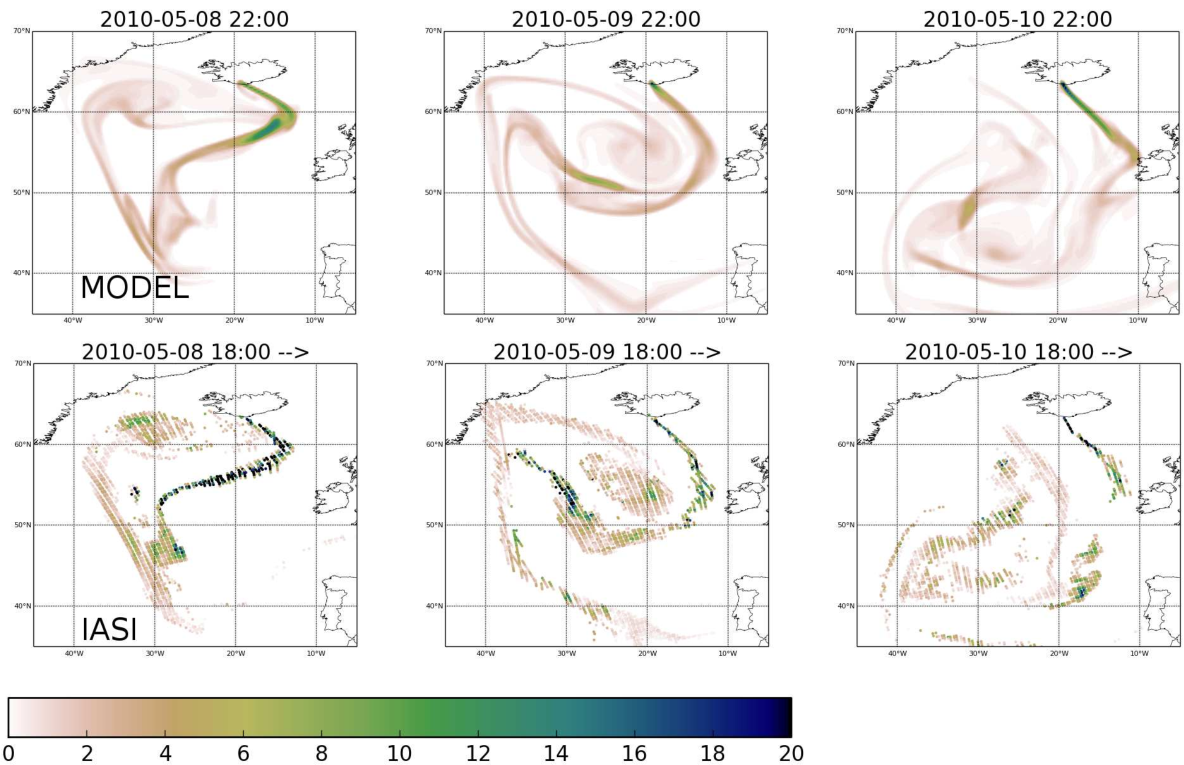

599
600 **Figure 12. As Figure 11, but 8-10 May, 2010.**

Geosci. Model Dev. Discuss., doi:10.5194/gmd-2016-200, 2016
Manuscript under review for journal Geosci. Model Dev.
Published: 15 September 2016

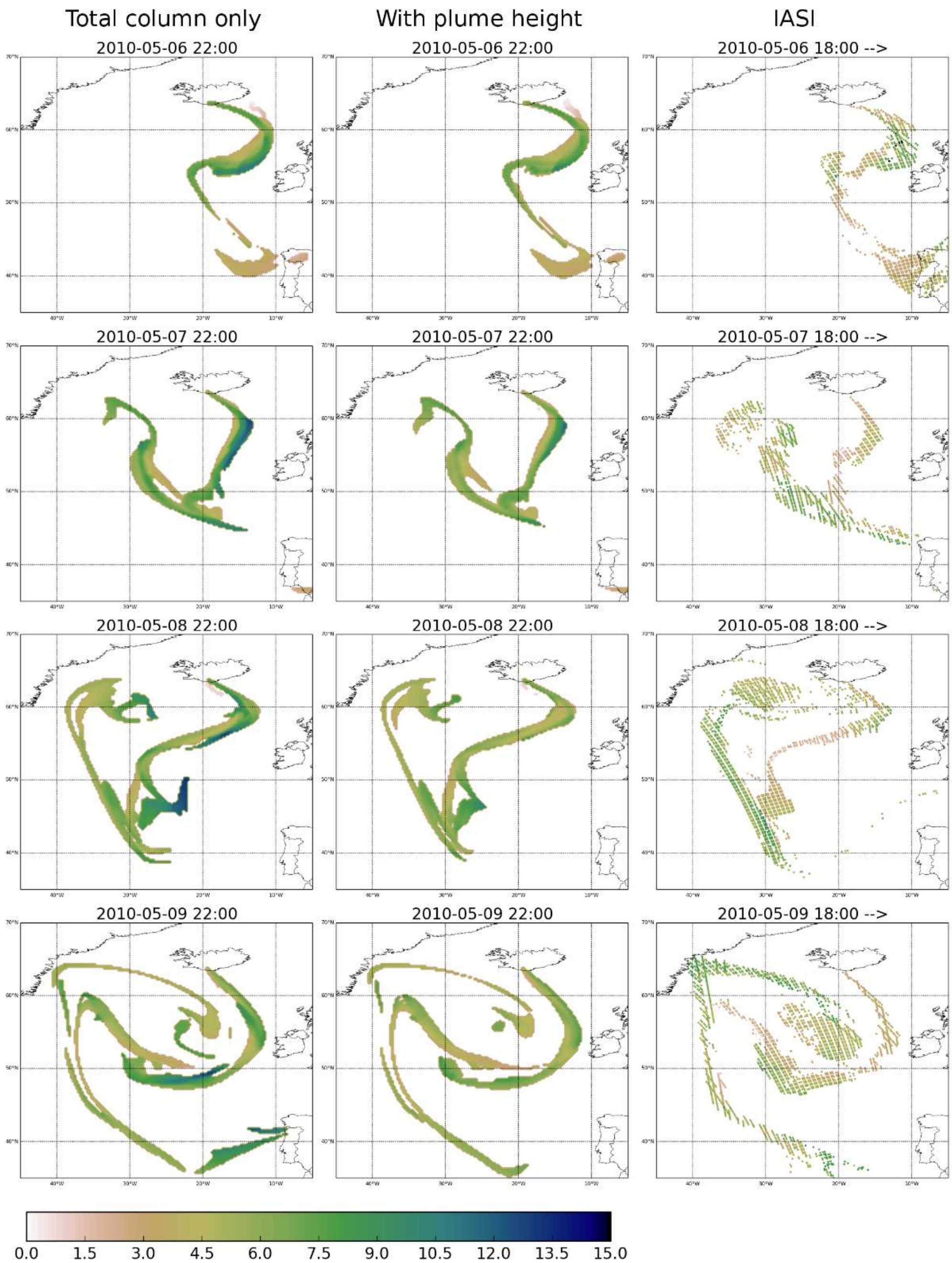

Figure 13. Simulated SO_2 plume height (centre of mass, km) without (left) and with (middle) assimilation of plume height retrievals for 6-9 (top to bottom row) May, 2010. The corresponding IASI retrievals are shown in the right column.